Bibliographical reference

Three Dimensional Motion Tracking of a Point on a Bowed Violin String Using High Speed Videography, Cheng-Zhong Zhang, Guang-Ming Zhang, Bang-Yan Ye and Li-Dong Liang, Acta Acustica **vol. 100** (Number 3), 2014, pp. 574-582

DOI

https://doi.org/10.3813/AAA.918736

Acta Acustica united with Acustica
Vol. 100 (2014) 574 – 582

DOI 10.3813/AAA.918736

Three Dimensional Motion Tracking of a Point on a Bowed Violin String Using High Speed Videography

Cheng-Zhong Zhang[1,2], Guang-Ming Zhang[3], Bang-yan Ye[2], Li-dong Liang[2]

[1] School of Software Engineering, South China Normal University, Foshan, 528225, China

[2] School of Mechanical and Automotive Engineering, South China University of Technology, Guangzhou, 510640, China

[3] General Engineering Research Institute, Liverpool John Moores University, Liverpool, L3 3AF, UK. g.zhang@ljmu.ac.uk

Summary

In order to understand the physics of a bowed violin string and develop an accurate model, experimental measurement of the bowed string motion is crucial. In this paper, a non-contact optical measurement system is designed to video the three dimensional motion of a point on a bowed string using a single high speed video camera. The designed system can directly record the string motion when bowing the strings fitted in violin without interference for movement. An imaging processing algorithm based on the circular Hough transform is then developed to process the recorded thousands sequential images, extracting the actual dynamic displacement of a fixed point on the string. Other string motion characteristics such as the velocity of the bowed string are further derived from the displacement waveforms. The tracked motion verified the predicted Helmholtz motion of the string. The experimental results show the superior performance of the proposed technique.

PACS no. 43.75.-z, 43.75.De, 43.75.Yy

1. Introduction

Modern research on the physics of a bowed string began with the discovery by Helmholtz, called as 'Helmholtz motion'. Raman then extensively investigated the characteristics of the Helmholtz motion [1] and string vibration mechanism, and presented a model to describe the dynamics of bowed string vibration [2]. Using this model, Raman was able to find various possible periodic string motions, including the Helmholtz motion. Thereafter, many studies on the bowed string mechanism have been carried out [3, 4, 5, 6, 7]. Recently, Knut Guettler analyzed the bowed string multi-phonics by use of the impulse response and Poisson summation formula [8]. In [9] a modal based identification technique, which enables the identification of the interface force as well as the string self-excited motion from the dynamical reactions measured at the string end supports, was developed by making use of inverse methods and optimization techniques.

The classic physical models for the bowed string motion are the stick-slip friction model and its variants [10, 11, 12], which were developed based on the Coulomb friction theory. Research suggests that the stick-slip model is too simple to describe the string motion, such as the frictional behavior of rosin. Therefore, other models such as thermal friction model [13], were attempted. A good review on the present state of knowledge about the mechanics of a bowed violin string can be found in [14, 15].

In order to understand the physics of a bowed string and develop an accurate model, experimental measurement of the bowed string motion is crucial. However, it is very difficult to directly measure the interaction between bow and string without interference for movement through experiment [9, 16, 17, 18].

In this paper, a non-contact optical measurement system on the basis of a single high speed video camera is designed to directly measure the three-dimensional motion of a point on the bowed string without interference for movement. The recorded sequential images are utilized to track the motion of an artificial marker on the string. The extracted motion data are further processed to analyze the dynamic displacement, trajectory, and velocity of a fixed point on the string.

2. Helmholtz motion of the bowed string

The Helmholtz theory predicts the motion of a bowed string as illustrated in Figure 1. Figure 1 shows snapshots of the string at successive instants in time. At all times it is formed of two straight-line segments. The breakpoint

Received 8 November 2013,
accepted 10 February 2014.

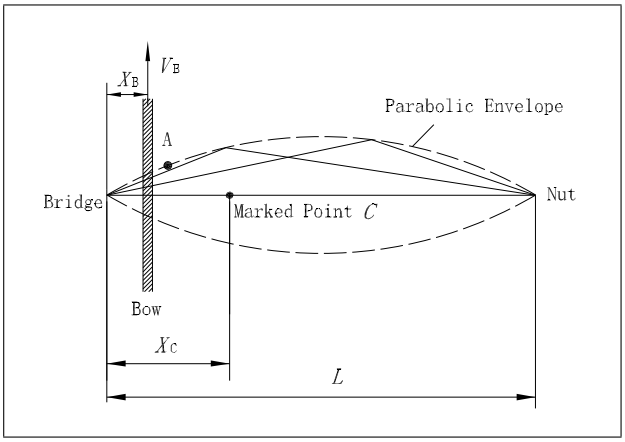

Figure 1. Principle of Helmholtz motion.

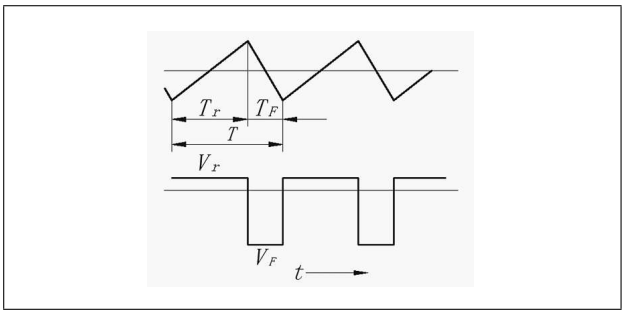

Figure 2. The Helmholtz motion of a given point in the bowed string. Upper: displacement; Lower: velocity.

between the segments propagates along the string at a uniform velocity and is reflected from the ends. The envelope of the breakpoints is a parabola [2].

Figure 2 shows the string motion as a function of time at a fixed point on a bowed string. Actually, at whatever point, its displacement follows a simple sawtooth triangle for an ideal Helmholtz motion. The velocity, in other words, stays at a constant positive value V_r during the rise time t_r, and at a constant value V_F during the fall time t_F. Helmholtz's analysis shows that the ratio of the fall time to the period T exactly equals the reduced distance X_C/L from the bridge to the point of observation (where L is the length of the string),

$$t_F/T = X_C/L. \tag{1}$$

This asymmetric waveform resulting from the phenomenon is often described as 'sticking and slipping'. There are certain departures observed in the motions of actual strings from the ideal motion of Figure 1. A number of the stick-slip friction models as mentioned in section 1 have been developed to describe the Helmholtz motion with a velocity dependent friction coefficient.

3. Experimental apparatus and methods

In order to track the three-dimensional motion of a point on a bowed string, a novel non-contact optical measurement system as shown in Figure 3 was designed. The

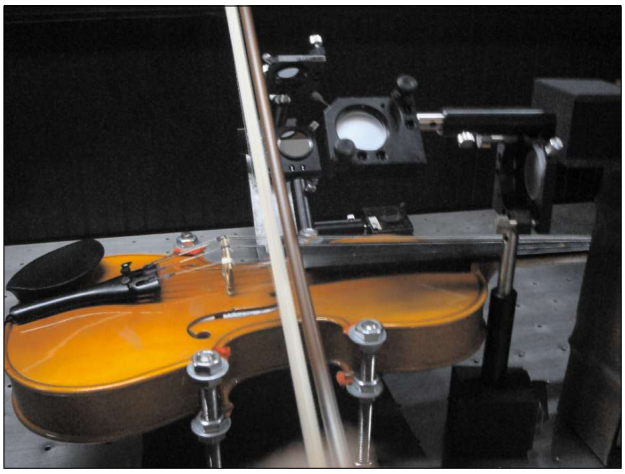

Figure 3. The experimental apparatus for 3D motion tracking of a point on a bowed string.

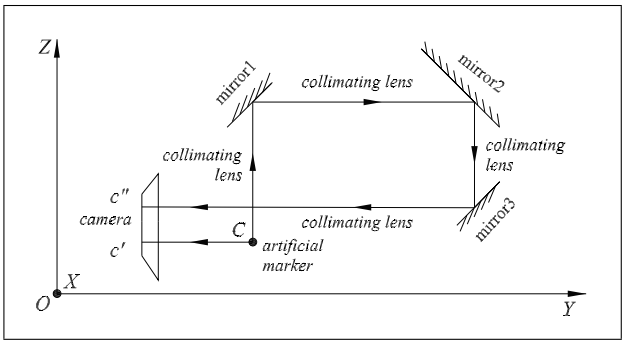

Figure 4. Schematic of the designed optical measurement system.

whole optical system is set up in an optical anti-vibration table. The video camera was placed by the table side using a tripod. For the convenience of our description, the coordinate system in the measurement system is defined as: X-axis is along the string direction in the horizontal plane, Y-axis is perpendicular to the strings in the horizontal plane, and Z-axis is the direction normal to the front plate. A tiny knot was tied in the interesting position of the violin string using a thin cotton thread. The knot was used as an artificial marker and its motion was tracked by the measuring system. In order to track the 3D motion of the marker using one video camera, an optical measurement system as illustrated in Figure 4 was designed. The vibration of the marker C in the X–Z plane is directly shot by the video camera. The vibration of the marker C in the X–Y plane was reflected to the camera lens through the optical path. The marker's projection c' in the X–Z plane and the marker's projection c'' in the X–Y plane were thus recorded simultaneously in a single image. The flat mirrors were carefully adjusted so that c' and c'' were separated with a suitable distance and both were in the focal plane of the camera lens. 3D motion characteristics of the marker can then be extracted through image processing which will be described in section 4.

A Fastec's HiSpce LTR2 high-speed digital video camera was used in our experiment. The camera is capable of

Table I. Parameters of the steel strings used in the violin. f_F: Fundamental frequency.

	Diameter [mm]	Tension [N]	f_F [Hz]
G	0.759	55.37	196
D	0.675	53.80	294
A	0.485	57.82	440
E	0.258	74.97	660

operating with recording speeds up to 500 frames per second (fps) at the full resolution of 1280×1024 pixels and optional frame rates exceeding 30,000 fps at a reduced resolution. The strings fitted in violin in the experiment are the Pirastro wire strings made in German, and their nominal parameters are shown in Table I. The string effective length is 328 mm, and the density of the G-string is $\rho = 3.1 \cdot 10^{-3}$ kg/m.

The string vibration was recorded when one of the strings were plucked or bowed. Figure 5 shows four examples of the recorded images when bowing the G-string. The marker's images were magnified to increase the accuracy of motion tracking by adjusting the camera view and the magnification of the camera lens. For each image in Figure 5, the upper part tracks the marker's motion in the X–Y plane, and the lower part tracks the marker's motion in the X–Z plane.

In our experiment, it is crucial to set up the frame rate and image resolution during videography, which have great impact on the accuracy of motion tracking. The frame rate is the sampling frequency in the time domain to the string motion. For the open G-string, the fundamental resonance frequency is 196 Hz as seen in Table I. If the frame rate is 7000 fps, 36 images will be recorded to track one vibration period T of the string motion as shown in Figure 2. At the full image resolution, the frame rate can only be 500 fps. As a result, in a vibration period only three images will be recorded. Three sampling points are difficult to describe one sawtooth accurately. Notice that the practical motion of the marker is not an ideal sawtooth waveform. In order to capture the details of the practical Helmholtz motion, high frame rates are required.

On the other hand, the image resolution determines the sampling frequency of the string motion in the spatial domain. If the image resolution is too low, the marker's positions in X-, Y-, and Z-directions in two or more time instants (i.e., in two or more consecutive images) will not be resolved, showing a constant position in these time instants. Thus, an optimal balance between the frame rate and image resolution has to be reached in order to obtain a high motion-tracking accuracy. In our experiment, the data were recorded at 6,650 fps with image resolution 336×480. This selection was obtained by trail-and-error, and might not be the optimal balance. Moreover, the frame rate setup depends on the total image pixels. Under a given total image pixel number, a trade-off exists between resolution in the x-axis and y-axis of the image. For example, the image resolution 336×480 is more appropriate than

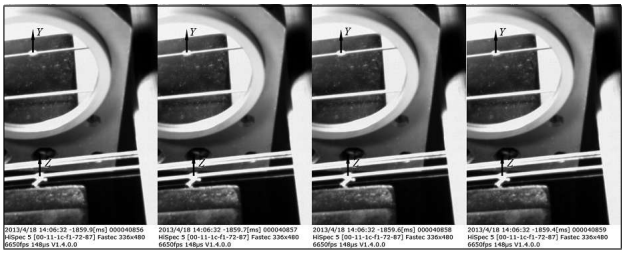

Figure 5. Four example images recorded when bowing the G-string. The upper white dot is the marker image in the X-Y plane, and the lower white dot is the marker image in the X–Z plane.

1280×126 because the dynamic displacement in the y-axis is bigger than in the x-axis, and a larger magnification of the camera lens can be used at the resolution 336×480. In addition, increasing the magnification of the camera lens can in some sense increase the accuracy of tracking the marker as well for a given image resolution and frame rate. However, it is not always available due to the space constraint of optical components setup.

4. Imaging processing for motion tracking of the artificial marker

The high-speed video data are saved as sequential images. In order to track the marker's motion, its centre position in every image is automatically extracted through image processing. The imaging processing procedure consists of five steps: 1) crop the recorded image to extract the regions of interesting (ROIs). Each ROI include only one marker image; 2) carry out thresholding operation on the cropped image; 3) enhance the cropped image; 4) extract the centroid locus of the marker using the circular Hough transform; 5) track the marker's positions in all time instants from the recorded sequential images.

Figure 6a shows a recorded image. In order to track the motion of the marker in the X–Z plane, we crop the recorded image in Figure 6a to extract the ROI which is the right-lower part. The cropped image is shown in Figure 6b. Then a thresholding operation is applied to the cropped image using equation (2),

$$I_\gamma = \begin{cases} 0, & \left| I_C(x,y) \right| < \gamma, \\ I_C(x,y) & \left| I_C(x,y) \right| \geq \gamma. \end{cases} \tag{2}$$

The threshold operation is used to remove the background noise. The threshold γ is set empirically in this paper. For our recorded images, since the marker's pixels have bigger intensity than the background, the threshold γ is set as 80% of the maximum intensity of the cropped image. The threshold operation removes the uninterested circle shape structures, so that the CHT will extract the centroid locus of the marker. If the threshold γ is set to a small value, a few centroid points from the uninterested structures might be obtained as well. In this case, position identification is needed to pick up the centroid locus of the marker in the fourth step. This can usually be done efficiently by searching the centriod locus in a given small region which is

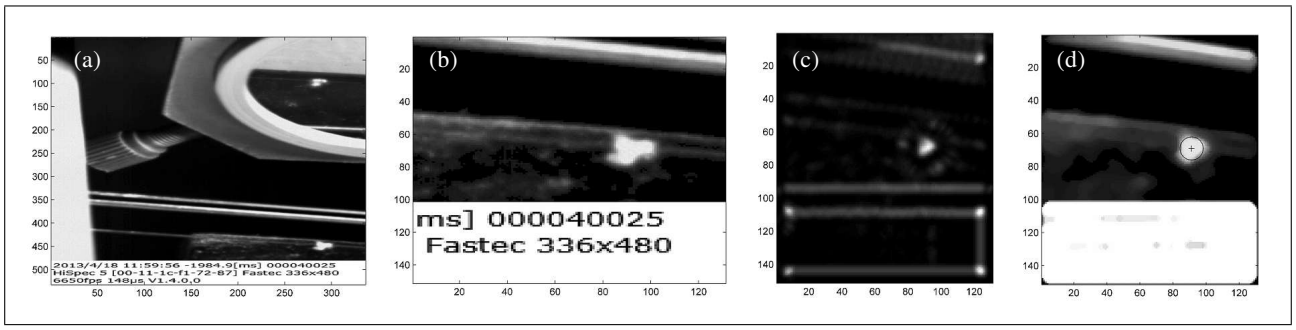

Figure 6. Detection of the marker's centre position. (a) A recorded image; (b) The cropped image; (c) The accumulation array image connected with the CHT; (d) The detected marker.

estimated according to equilibrium position and the dynamic range of the displacement of the marker. In the third step, filtering operation is used to smooth the thresholded image. 2-D median filtering was performed in this paper. Notice that histogram equalization can be further used to enhance the image in this step if it is needed. Histogram equalization tends to increase the contrast of the image and produced a better result for region-based feature extraction. In this paper, no histogram equalization is applied.

A gradient based Circular Hough Transform (CHT) is used to extract the marker's centre position. The Hough Transform (HT) defines a mapping from the image points into an accumulator space (Hough space) based on the function that describes the target shape [19, 20, 21]. The CHT reformulates the explicit circle equation into parametric form, with two parameters: circle radius r and circular angle θ. The equation of a circle and HT mapping used is as

$$\left(x - x_0\right)^2 + \left(y - y_0\right)^2 = r^2, \tag{3}$$

$$x_0 = x - r\cos\theta, \quad y_0 = y - r\sin\theta, \tag{4}$$

where (x, y) denote a point locus, and (x_0, y_0) denote the origin of the circle. Before the CHT, the gradient field of the image is calculated using equation (5) and used to define the edge of the circular object,

$$\nabla I_\gamma(x, y) = \frac{\partial I_\gamma(x, y)}{\partial x}\boldsymbol{i} + \frac{\partial I_\gamma(x, y)}{\partial y}\boldsymbol{j}, \tag{5}$$

where $\nabla I_\gamma(x, y)$ is the intensity gradient function of two variables (x, y), $\boldsymbol{i}$ is the unit vector in the x-axis and $\boldsymbol{j}$ is the unit vector in the y-axis. The circular Hough Transform (HT) is then carried out on the thresholded image $I_\gamma(x, y)$. The gradient based circular Hough transform resolves the centroid locus and the radius of the artificial marker. The Hough transform has been generalized to detect arbitrary shapes as robust techniques [21]. Notice that suitable parameters in the CHT algorithm should be set to eliminate false detection. Figure 6c shows the accumulation array which is generated in CHT. Figure 6d shows the detected marker. Similarly, the marker in the top-right corner of Figure 6a can be detected, and the marker's centroid locus in the X–Z plane can then be detected.

In this study, we are only interested in the marker's centroid locus, and the radius of the marker is not our concern. Moreover, we would like to point out that the CHT can detect the marker's centroid locus at sub-pixel resolution, which is very important in this experiment. The sub-pixel resolution is achieved in the Hough transform because the marker's centroid locus is calculated through the detected marker's edge. Although the marker's centroid locus might be in the same pixel in two digital consecutive images, some of the points in the marker's edge might be crossed to a neighbouring pixel due to the vibration in the two consecutive time instants. This is intuitively explained as follows: suppose a 10 times higher resolution video camera is used to video the same marker, each pixel in the marker's edge of the original image now becomes 10 pixels. Assume an edge point with centre locus $y = 10$ in the original image. The centre locus of the point should be located in between $y = 100$ to 110 in the higher resolution image. If $y = 109$ in the higher resolution image and the marker moves two pixels in the next time instant, the centre locus of the point then becomes $y = 111$ in the high resolution image. As a result, the edge point's position becomes $y = 11$ in the original image. Obviously, the sub-pixel capability depends on the size of the marker image. Study of the sub-pixel capability in depth is out of the scope of this paper. In fact, the commercial motion tracking software normally has sub-pixel capability, for example the one used in [22] has ten subdivisions within each pixel.

The image processing algorithm described above was implemented in the MATLAB environment. The recorded sequential images were processed as a batch. In addition, when cropping the images, the cropped image size should be big enough to avoid the marker is out of the cropped image when the marker vibrates to its maximum displacement. Finally, the 3D motion tracking of the marker is obtained by assembling the obtained centroids.

5. Experimental results and discussions

5.1. Motion tracking of a plucked string

The response of a plucked string with rigidly fixed ends is a standard textbook problem [23]. The plucked string would have a series of resonances with approximately harmonic spacing. The frequencies will not be exactly harmonic because of the effect of bending stiffness. Each

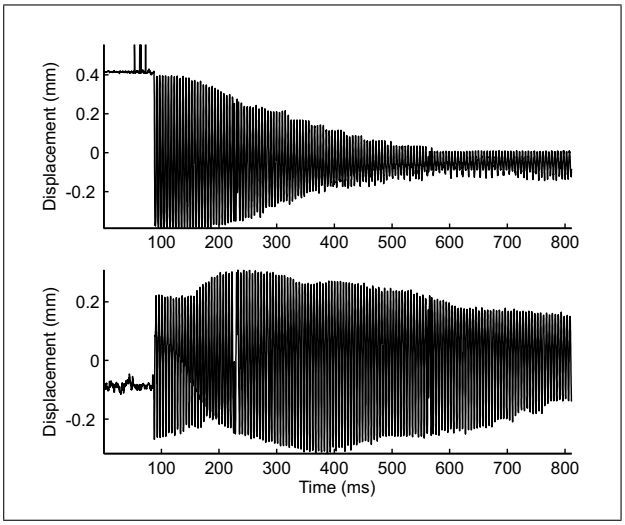

Figure 7. Motion scenarion of the artificial marker when plucking the open G-string. Top: displacement at Y-direction, Bottom: displacement at Z-direction.

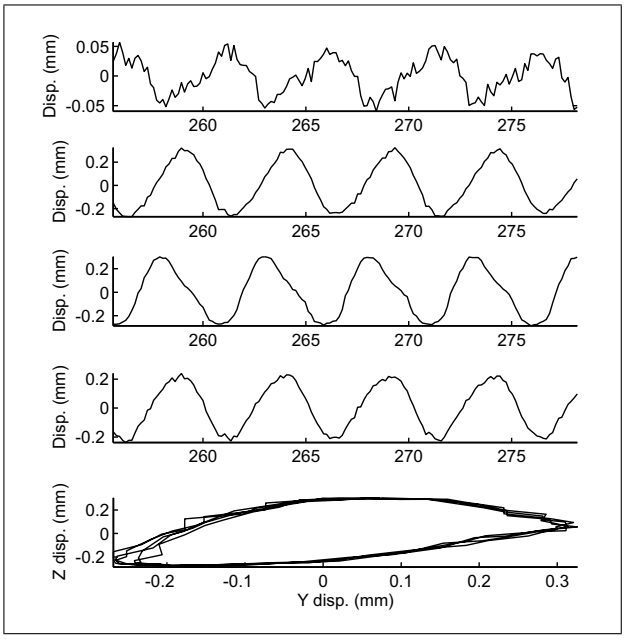

Figure 8. Motion of the artificial marker when plucking the open G-string. Close-look. From top to bottom: Displacements at X-, Y- and Z-direction, total displacement, motion trajectory in the X–Z plane.

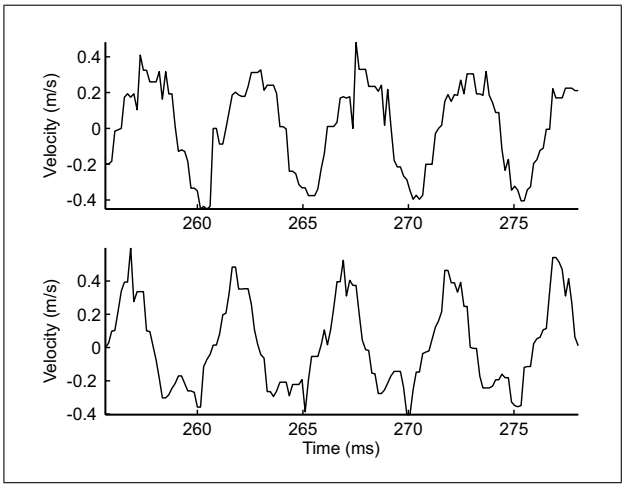

Figure 9. Velocity of the artificial marker when plucking the open G-string. Top: velocity at Y-direction, Bottom: velocity at Z-direction.

string harmonic is a pair of modes, because the string can vibrate in two different polarization planes. When the string is couple to the violin body through the bridge, this set of string modes will couple to the set of modes of the violin body. For each harmonic of the string motion one expects to see two modes, with different damping factors because of the body coupling [24].

The motion of the artificial marker measured in our experiment during plucking the open G-string is plotted in Figures 7–11. The marker is located at 64 mm away from the bridge. The string was plucked with a finger at 130 mm location away from the bridge. The displacement data extracted using the proposed image processing algorithm from 5395 sequential images are plotted in Figure 7, showing the motion scenario. The initial plucking displacement can be seen from the beginning of the waveforms in Figure 7, having displacement components in both the X–Y plane and the X–Z plane. Thus, the plucking direction is not strictly along the Y-direction. Notice that the displacements extracted from the recorded images are in pixels. Through experimental calibration, the pixels were then converted into millimeter. According to our calibration, one pixel equals 0.0264 mm in this experiment.

Figure 8 shows a close look of the displacement waveforms extracted from Figure 7. The total displacement waveform in Figure 8 was obtained by combining the displacement components at the X-, Y- and Z-directions. The corresponding motion trajectory is plotted in Figure 8 as well. The velocity waveforms of the artificial marker derived by differential operation from the displacement waveforms are shown in Figure 9. Three points median filtering is applied to these derived velocity waveforms to remove the noise caused by the differential operator. Figure 10 plots the trajectory in the velocity-displacement plane, called as 'phase trajectory'. The phase trajectory is often used to characterize the dynamic vibration.

The frequency response of the plucked string, which was obtained by applying out the Fast Fourier Transform to the displacement waveforms in Figure 7, is presented in Figure 11. Notice that the bandwidth of the proposed measurement system is determined by the recording speed of the video camera if the image resolution is good enough to resolve the spatial motion of the marker in the consecutive time instants as described in section 3. From Figure 8, it can be seen that the image resolution is appropriate in our experiment because if the image resolution is not high enough, small steps should be seen in the displacement waveforms. In Figure 11, nine harmonics are observed in the Z-direction; however only three harmon-

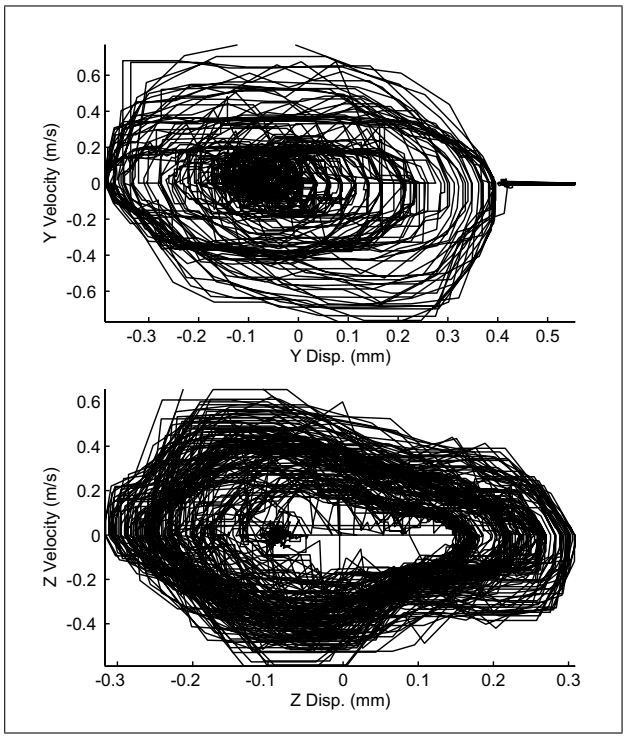

Figure 10. Phase trajectory of the artificial marker when plucking the open G-string. Top: trajectory in the Y–Vz plane, Bottom: trajectory in the Z–Vz plane.

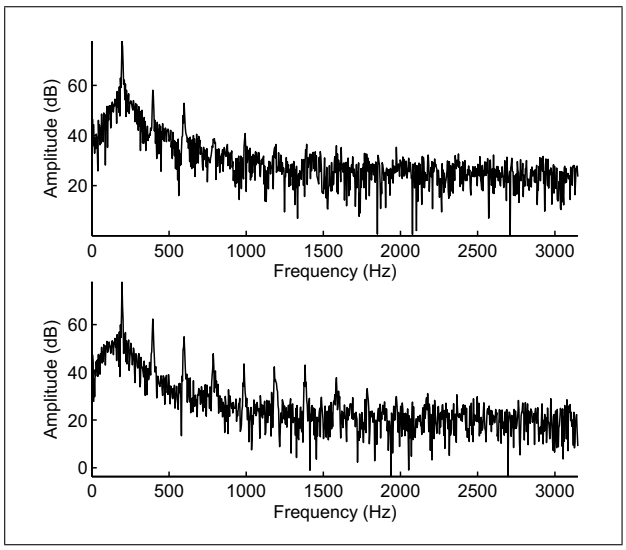

Figure 11. Frequency response of the artificial marker when plucking the open G-string. Top: Y-direction, Bottom: Z-direction.

ics are clearly observed in the Y-direction. Further investigation is needed to clarify this observation.

It is also interesting to note that the attenuation in the Y-direction is much quicker than in the Z-direction according to Figure 7. This might be due to: 1) the damping factors in the two directions are different; 2) energy transfer from the Y-direction to the Z-direction, something that is clearly plausible, accounting for the bridge/sound-post coupling effects on the string dynamics.

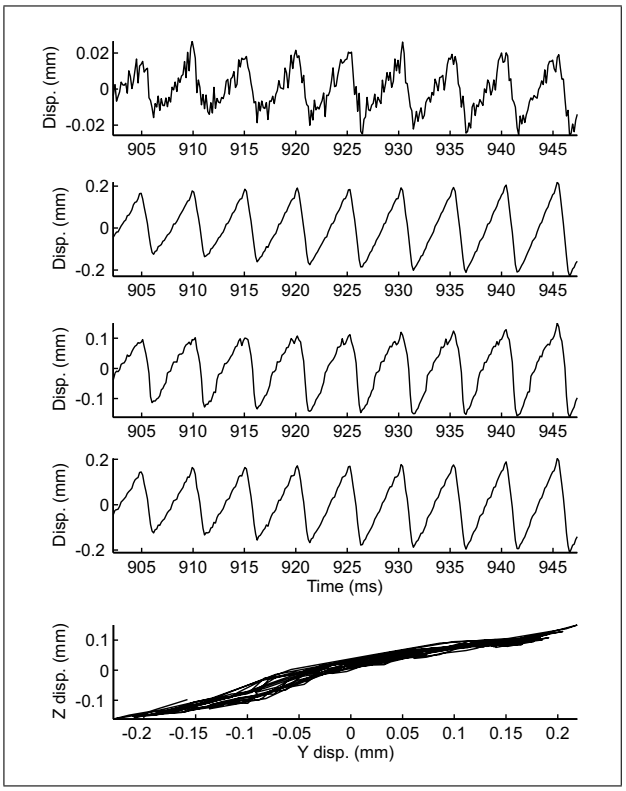

Figure 12. Motion of the artificial marker when bowing the open G-string. From top to bottom: Displacements at X-, Y- and Z-direction, total displacement, motion trajectory in the Y–Z plane.

In addition, the displacement waveforms in Figure 7 are the transient responses of the marker in the Y- and Z-directions. The polarization behavior of the string motion mentioned above could be investigated from these displacement waveforms. Study of the string motion in depth using the proposed measurement method is out of the scope of this paper.

5.2. Motion tracking of a bowed string

In this experiment, the strings were bowed by a violin player. The bow was bowed along the Y-direction towards the positive Y-direction in the X–Y plane in the coordinate system as defined in section 3. If the bowing direction is along the negative Y-direction, the extracted Y-directional displacement waveform in the proposed measurement system should be reversed. The distance from the bow-string contact position to the bridge is 30 mm. The motion of the artificial marker when bowing the open G-string is shown in Figures 12–15. The marker was located at 64 mm away from the bridge. The displacement waveforms in the X-, Y-, Z-directions were obtained by processing 7101 sequential images recorded using the proposed measurement system in section 3. Figure 12 shows the typical displacement waveforms in the X-, Y-, Z-directions. For an ideal string mounted on an ideal monochord, the motion of bowed string can be regarded as the plane vibration, only the transverse vibration should normally be considered. In practice, real strings mounted on instrument bod-

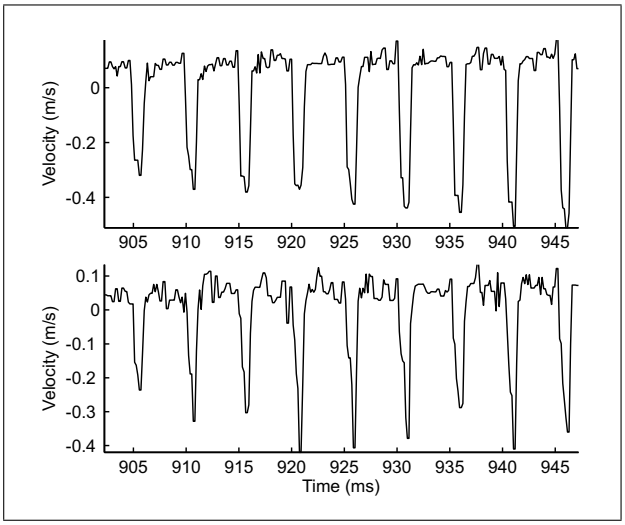

Figure 13. Velocity of the artificial marker when bowing the open G-string. Top: velocity at Y-direction, Bottom: velocity at Z-direction.

ies will display coupling effects between the $Y(t)$ and $Z(t)$ responses. In addition, the focal axis of the camera is not guaranteed to be strictly along the Y-direction in our experiment setup. It is also not guaranteed that the bowing direction is kept strictly along the Y-direction in all the time instants due to minor instability of bowing the string. Thus, small displacement in the X-direction is observed. The total displacement waveform in Figure 12 is obtained by combining the three displacement components at the X-, Y- and Z-directions. From Figure 12, the transverse movement of the violin string is a sawtooth waveform, which agrees with the Helmholtz motion in Figure 2.

From the total displacement waveform, the averaged vibration period is 5.08 ms. Thus, the vibration frequency of the string is 197Hz, which is very close to the fundamental frequency 196Hz expected from the excited G-string. Furthermore, the Helmholtz motion equation (1) is verified from the total displacement waveform. The estimated T_F is equal to 1 ms. Thus, $T_F/T = 0.197$ which is very close to $X_c/L = 64/328 = 0.195$.

The motion trajectory in the Y–Z plane is plotted in Figure 12 as well. The trajectory should be consistent with the bow movement projected to the Y–Z plane. The derived velocity waveforms from Figure 12 are plotted in Figures 13. Figure 14 shows the trajectory of displacement versus velocity. These results in Figures 12–15 agree very well with the findings in the literature. For example, the trajectory of displacement versus velocity in Figure 14 fairly agrees with the model prediction in the literature [11].

The frequency response of the bowed string, which was obtained by applying out the Fast Fourier Transform to the displacement waveforms, is presented in Figure 15. Up to the 8th harmonic is clearly observed in both the Y- and Z-directions in Figure 15.

The displacement waveforms in Figure 12 also demonstrate the sub-pixel capability of the proposed image processing algorithm. Notice that there are 34 sampling points in time for one sawtooth period in the presented results. The string moves less than 2 pixels at the X-direction, 15 pixels at the Y-direction, and 10 pixels at the Z-direction in Figure 12. Without sub-pixel capability, the sawtooth shape would not be resolved in the X-directional displacement waveform.

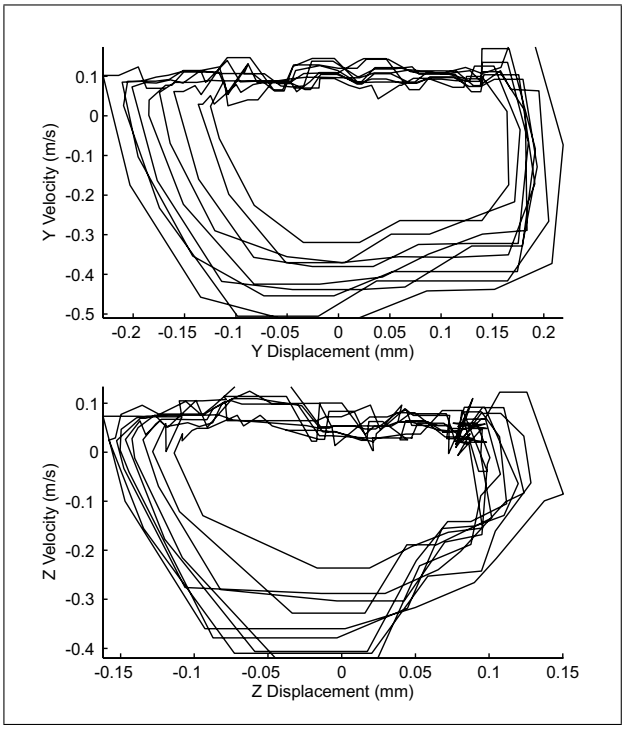

Figure 14. Displacement versus velocity of the artificial marker when bowing the open G-string.

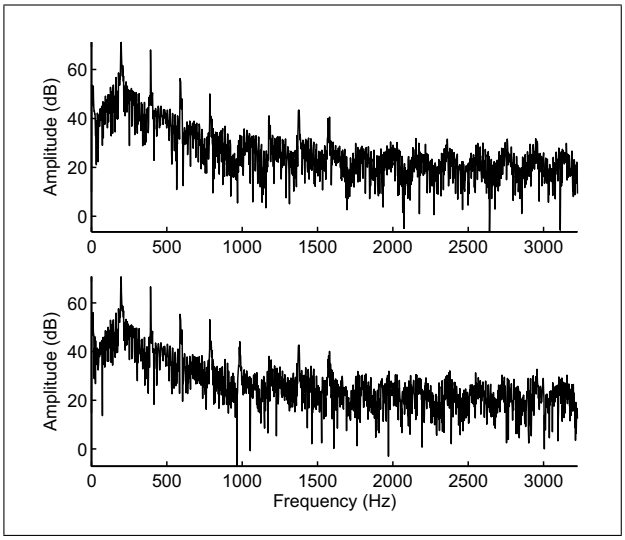

Figure 15. Frequency response of the artificial marker when bowing the open G-string. Top: Y-direction, Bottom: Z-direction.

5.3. Discussions

The major features of the proposed measurement technique are discussed as follows:

1. Measure the three dimensional motion of a string. A similar work has been presented in [22], where a high speed video camera was used to track the violin string motion. Our measurement results seem to be much better than the results presented in [22]. The method in [22] measures only one plane motion. Although the string is normally considered to be plane vibration, the three dimensional motion can provide us some additional information. For example, Figure 16 shows a further close-look to the displacement waveforms in Figure 12. It is interesting to note that the Y-directional displacement waveform is nearly an ideal Helmholtz motion but there are departures at the Z-direction, particularly in the corner of the sawtooth. Moreover, if the focal axis of the camera is not perpendicular to the X-axis, the motion measured in one plane will be a projection of the string motion in other plane rather than the transverse plane.
2. The proposed measurement is non-contact, and the string motion can be tracked without interference with the string vibration. Moreover, unlike the popular magnetic violin pickup which can only be used for metal strings, the proposed technique can be used to track the motion of any types of strings for example the nylon string. In addition, for the magnetic violin pickup, the finite length of the magnetic field will affect the tracking accuracy. For the proposed system, the motion of a single point on the string can be accurately tracked due to the benefits of the tiny cotton marker and image processing algorithm.
3. The tiny cotton marker on the string is of benefit to the tracking accuracy. In [22], no marker has been made on the string, and the recorded video data were imported into commercial software for motion analysis. The commercial software normally tracks the motion of an interesting point by tracking an image point with a fixed X- position in the string of an image rather than a physical point in the physical string. This might generate significant errors for motion analysis because in practice the X-position of the physical point in the string will dynamically change as seen in Figure 12 if the camera focal axis is not in the transverse plane of the string vibration. In the proposed system, we track the motion of a physical point in the string.
4. The image processing algorithm is of benefit to the tracking accuracy due to its sub-pixel resolution.
5. By tracking the motions of multiple artificial markers on the string, the propagation of the wave through the string can be directly studied.
6. As discussed in section 5.1, the bandwidth of the proposed measurement technique is mainly determined by the recording speed of the video camera, thus it is limited. There are many other non-intrusive techniques that have been used to measure the motion of the bowed strings in the literature, such as magnetic pickup, accelerometer/force sensor or laser vibrometer. Each of these measurement techniques has their own advantages and limitations, suitable for a particular study. For example, the force sensor has been embedded in the bridge, monitoring the transverse force exerted by the moving string. It has been shown to have a very high bandwidth, but it cannot track the motion of a point on the bowed string directly. A comparison study for the performance of all these techniques would be interesting and useful, but out of the scope of this paper.

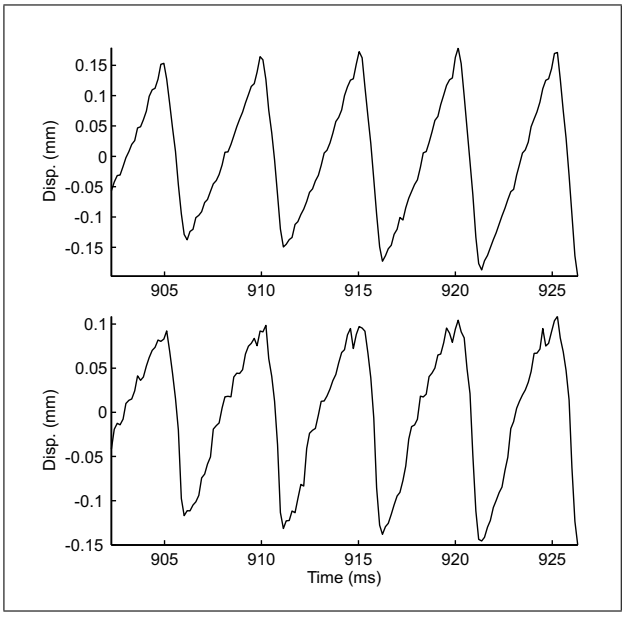

Figure 16. Close look of the displacement waveforms extracted from Figure 12. Top: displacement at Y-direction, Bottom: displacement at Z-direction.

6. Conclusions

In this paper, a high speed video camera based non-contact optical measurement system has been designed for accurately measuring the displacement of a string when plucking or bowing a string fitted in violin. The designed system can record three dimensional motion of the plucked/bowed string. A circular Hough transform based image processing algorithm has then been developed to process the recorded sequential images for motion analysis. The developed image processing algorithm can extract the centroid locus of an artificial marker on the string at sub-pixel resolution. The superior performance of the developed technique has been demonstrated by experiment. The tracked motion has verified the predicted Helmholtz motion of the string. The proposed technique provides a tool to study the physics of a bowed string experimentally, for example the impact of rosin. The tracking results presented in this paper can be further improved by using a better video camera and a better lens, and an optimal balance between the frame rates and image resolution.

References

[1] C. V. Raman: The dynamical theory of the motion of bowed strings. Indian Assoc. Cult. Sci. Bull. (1914) 43–52.

[2] C. V. Raman: On the mechanical theory of bowed strings. Indian Assoc. Cult. Sci. Bull. **15** (1918) 1–158.

[3] F. G. Friedlander: On the oscillations of the bowed string. Proc. Cambridge Phil. Soc. **49** (1953) 516–530.

[4] J. Kohut, M. V. Mathews: Study of motion of a bowed violin string. J. Acoust. Soc. Am. **49** (1971) 532–537.

[5] B. Lawergren: On the motion of bowed violin strings. Acustica **44** (1980) 194–206.

[6] M. E. McIntyre, J. Woodhouse: Friction and the bowed string. Wear **113** (1986) 175–182.

[7] J. Woodhouse: On the stability of bowed string motion. Acustica **80** (1994) 58–72.

[8] K. Guettler, H. Thelin: Bowed-string multiphonics analyzed by use of impulse response and the Poisson summation formula. J. Acoust. Soc. Amer. **31** (2012) 766–772.

[9] V. Debut, X. Delaune, J. Antunes: Identification of the nonlinear excitation force acting on a bowed string using the dynamical responses at remote locations. International Journal of Mechanical Sciences **52** (2010) 1419–1436.

[10] J. Woodhouse, R. T. Schumacher, S. Garoff: Reconstruction of bowing point friction force in a bowed string. J. Acoust. Soc. Amer. **108** (2000) 357–368.

[11] R. I. Leine, D. H. Van Campen, A. De Kraker, L. V. D. Steen: Stick-slip vibrations induced by alternate friction models. Nonlinear Dynamics **16** (1998) 41–54.

[12] A. Akay: The acoustics of friction. J. Acoust. Soc. Amer. **111** (2002) 1525–1548.

[13] J. Woodhouse: Bowed string simulation using a thermal friction model. Acta Acustica united with Acustica **89** (2003) 355–368.

[14] J. Woodhouse, P. M. Galluzzo: The bowed string as we know it today. Acta Acustica united with Acustica **90** (2004) 579–589.

[15] J. Woodhouse: Idealised models of a bowed string. Acustica **79** (1993) 233–250.

[16] R. T. Schumacher, S. Garoff, J. Woodhouse: Probing the physics of slip-stick friction using a bowed string. The Journal of Adhesion **81** (2005) 723–750.

[17] R. T. Schumacher: Studies in bowing-point friction in bowed strings. J. Acoust. Soc. Am. **103** (1998) 2915.

[18] M. D. Araújo, J. Antunes, P. Piteau: Remote identification of impact forces on loosely supported tubes. part1: Basic theory and experiments. Journal of Sound and Vibration **215** (1998) 1015–1041.

[19] M. Nixon, A. S. Aguado: Feature extraction & image processing. Hough transform. Newnes, Oxford, 2002. 173-213.

[20] M. Rizon, Y. Haniza, S. Puteh et al.: Object detection using circular Hough transform. American Journal of Applied Sciences **2** (2005) 1606–1609.

[21] D. H. Ballard: Generalizing the Hough transform to detect arbitrary shapes. Pattern Recognition **13** (1981) 111–122.

[22] C. V. Karsen, T. Bouman, G. Gwaltney: Operating deflection shapes of a violin string via high speed/high resolution videography. Topics in Modal Analysis, Volume 7: Conference Proceedings of the Society for Experimental Mechanics Series 45, 2014, 637–644.

[23] L. Cremer: The physics of the violin. MIT Press, Cambridge, MA, USA, 1984. Chapter 2.

[24] J. Woodhouse: Plucked guitar transients: comparison of measurements and synthesis. Acta Acustica united with Acustica. **90** (2004) 945–965.